Received: 19 March 2018 | Revised: 19 June 2018 | Accepted: 20 June 2018

DOI: 10.1002/jrs.5450

RESEARCH ARTICLE

WILEY Journal of RAMAN SPECTROSCOPY

Optical sectioning in multifoci Raman hyperspectral imaging

Zhiyu Liao[1] | Faris Sinjab[1] | Hany M. Elsheikha[2] | Ioan Notingher[1]

[1]School of Physics and Astronomy, University of Nottingham, Nottingham, UK

[2]School of Veterinary Medicine and Science, University of Nottingham, Leicestershire, UK

Correspondence
Ioan Notingher, School of Physics and Astronomy, University of Nottingham, Nottingham NG7 2RD, UK.
Email: ioan.notingher@nottingham.ac.uk

Funding information
Engineering and Physical Sciences Research Council, Grant/Award Numbers: EP/L025620/1 and EP/M506588/1

Abstract

In this study, we compared the depth discrimination and speed performance of multifoci Raman hyperspectral imaging with the reference standard of a single laser point confocal Raman mapping. A liquid crystal spatial light modulator was employed for the generation of multifoci laser beams, and a digital micromirror device was used as a software-configurable reflective pinhole array. The patterns of the laser foci and pinhole array can be rapidly changed without requiring any hardware alterations. Confocal patterns with different distance-to-size ratios were tested and compared. After optimization of the laser-foci pattern, we demonstrated the feasibility of multifoci Raman hyperspectral microscopy for recording depth-resolved molecular maps of biological cells (*Acanthamoeba castellanii* trophozoites). Micrometric depth discrimination and short acquisition times (20 min for single plane confocal image) were achieved.

KEYWORDS

confocal Raman imaging, cross-talk, multi-beam, optical sectioning, single cell imaging

1 | INTRODUCTION

Raman microspectroscopy (RMS) is a powerful technique for highly specific molecular imaging of samples in three dimensions (3D).[1] RMS instruments typically utilize a single laser beam to excite Raman scattering at a sample, which is analyzed by a spectrometer, with hyperspectral images formed by raster-scanning the laser spot and obtaining a Raman spectrum at each point. A pinhole is often placed at the spectrometer entrance to ensure confocal measurement configuration for improved depth discrimination. Although RMS allows sensitive and chemically specific hyperspectral imaging, acquisition times for measurements in 3D are often lengthy, due to the weak spontaneous Raman scattering cross section of many materials. The addition of a pinhole also typically comes at the cost of optical throughput for RMS detection, further increasing the acquisition times.

Several techniques have been proposed and demonstrated for achieving fast Raman spectral mapping, such as line- or slit-scanning[2,3] and wide-field Raman imaging.[4,5] Compared with confocal single-beam scanning Raman imaging, these power-sharing Raman imaging techniques effectively shorten the mapping time by measuring multiple sample locations simultaneously. However, both line-scanning and wide-field techniques tend to decrease the depth discrimination because of decreased or lack of confocality. Multifoci excitation is a promising strategy to improve Raman imaging speed while maintaining good depth discrimination.[6–12] Raman spectra from these

illuminated laser spots are simultaneously collected at a two-dimensional (2D) detector (e.g., charge-coupled device [CCD] camera) after undergoing some form of spatial filtering to ensure depth discrimination. If the generated multifocal points are sufficiently separated from each other in the sample plane, the cross-talk caused by overlapping of laser beams and diffuse scattering of Raman photons reaching the detector can be reduced. Thus, the confocality of the individual Raman spectra could be maintained, and the acquisition time was reduced by a factor equal to the number of laser foci compared with single-beam confocal Raman microscopy. This approach has high potential for speeding up confocal Raman mapping as lasers with powers in the order of 1–10 W are available and could be used to generate tens of laser foci.

There are several methods reported in the literature for generation of multifoci beams, including the use of a microlens array,[6] diffractive optical elements,[9,12] galvomirrors,[13] and spatial light modulator.[8,14] If the multifocal pattern is a line, the scattered Raman photons can be simply imaged on the spectrometer slit to generate spatially resolved Raman spectra in one dimension (1D) of a CCD detector (perpendicular to the dispersion direction). If the multifocal pattern is 2D, typically, a fiber bundle is used to rearrange the Raman photons into a 1D array for coupling into the spectrometer. Recently, Yabumoto and Hamaguchi reported a novel method to achieve multifocal Raman imaging.[12] Instead of using a fiber bundle, a pair of periscopic mirrors were used to precisely tilt the square pattern of signals so that Raman signals from different foci do not overlap on the detector, with masking pinhole array was used to ensure confocality. Kong et al. developed a time-sharing 2D multifocal Raman imaging system using galvomirrors.[13] The use of a rigid multiconfocal array was avoided by combining a galvomirror-based parallel detection and Hadamard transform detection. Recently, we have developed a technique based on spatial light modulators for multifoci Raman microscopy.[15] This approach relies on a liquid crystal spatial light modulator (LC-SLM) to generate a desired pattern of laser foci and employs a digital micromirror device (DMD) in the detection path to function as a software-configurable reflective pinhole array. Because both the SLM and the DMD can be easily controlled through software, the positions of the laser foci can be rapidly changed without requiring any hardware alterations. The feasibility and versatility of DMD as reflective pinholes were also demonstrated for spatially offset Raman spectroscopy.[16,17]

A limitation of multifoci Raman mapping is that the practical number of laser foci is limited by the small field of view of the high numerical aperture (NA) objectives used in confocal Raman microscopy. A high NA objective is required to maximize depth discrimination and increase the collection of Raman photons. As a consequence, the laser foci have to be placed closer together. The overlapping laser light corresponding to different foci leads to cross-talk between the Raman spectra detected on the CCD and thus degrades the depth discrimination.

In order to optimize the measurement configuration for multifoci confocal Raman spectroscopy, we investigated the influence of the distance between adjacent laser foci on the depth discrimination of multifoci confocal system. The combination of LC-SLM and DMD in the Raman microscope provided the flexibility to modify the number, location, and spacing between the laser foci in software without altering any optical components in the system. This allows the changes in the recorded Raman hyperspectral images, such as depth discrimination with different 2D multifocal patterns to be investigated easily.

In the present study, we compared the depth discrimination and speed performance of different 2D multifocal patterns with the reference standard of single laser point confocal Raman mapping. After optimization of the laser foci pattern, we demonstrated the feasibility of recording depth-resolved Raman maps of biological cells.

2 | MATERIALS AND METHODS

2.1 | Sample preparation

Olive oil sample (referred in the paper as "oil") was obtained from a local shop. The preparation of diphenylalanine (FF) microtubes is described elsewhere.[18] The size of the prepared tubes ranged from a few to tens of micrometers in diameter. The tubes were transferred to a quartz slide by depositing a droplet of the diluted stock solution. Water was evaporated before measurements. The culture of *Acanthamoeba castellanii* trophozites was maintained in peptone yeast glucose medium in tissue culture flask at 25°C as described previously.[19] Trophozites were seeded into quartz slide (thickness 0.17 mm) for a few hours, followed by fixation in 4% paraformaldehyde for 30 min. Then, paraformaldehyde was removed, and the fixed trophozites were maintained in phosphate-buffered saline solution at 4°C, until used in imaging.

2.2 | Apparatus

A brief diagram of the multifoci Raman microscope system is shown in Figure 1. A CW Ti:Sapphire laser (SpectraPhysics) at 785 nm was expanded to illuminate the active area of an LC-SLM. The multifoci beam pattern was produced by generating a phase hologram in LabVIEW and displaying it on the LC-SLM.[20] The modulated laser beams were then focused onto the sample by

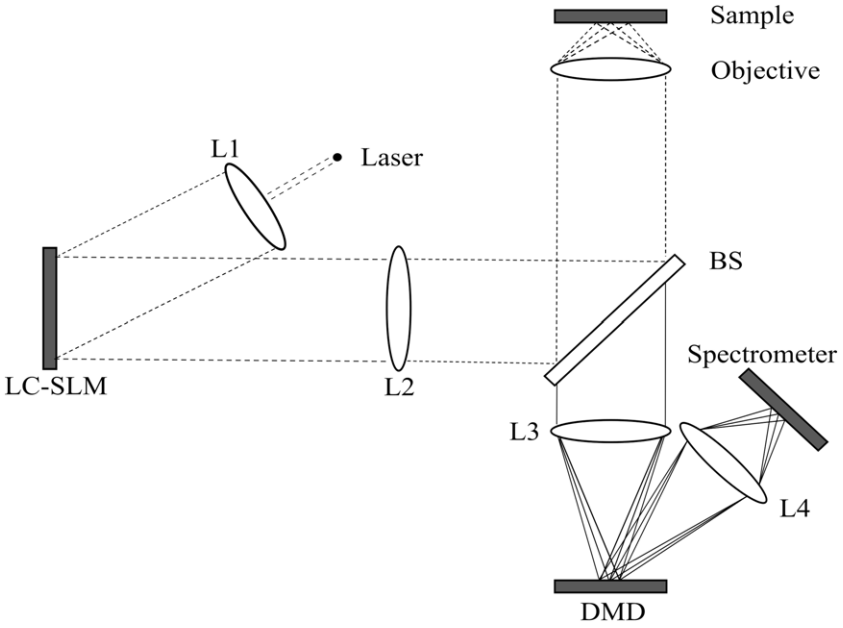

FIGURE 1 Schematic diagram of the multifoci confocal Raman microscope. BS: beam splitter; DMD: digital micromirror device; L1: beam expander; L2: telescope relay; L3 and L4: lens groups; SLM: liquid crystal spatial light modulator

a 60×/1.2 NA water-immersion objective (Olympus, Japan). Raman scattered light from the multiple spots was collected by the same objective and focused onto a DMD (DLP LightCrafter, Texas Instruments). The latter functions as a reflective confocal pinhole array to direct only the signal from the multifocal sampling points into the spectrometer (Acton LS 785, Princeton Instruments). The synchronization of the DMD was controlled using a LabVIEW plugin for the RedTweezers software so that any changes in the beam pattern would automatically generate a matching pinhole pattern in real time.

3 | RESULTS AND DISCUSSION

First, we investigated four multifoci beam patterns, with the adjacent aperture distance-to-size ratio gradually increased from $R = 2$ to $R = 16$, using a uniform polystyrene slide and a thick transparent sample (oil), in order to understand the effect of the laser foci overlap and signal cross-talk on the depth discrimination in multifoci Raman spectroscopy (Figures 2 and 3). The $R = 2$ period denotes that the distance from the center of a pinhole to the center of an adjacent one is twice the size of the pinhole itself (see Figure 2a). The $R = 8$ pattern was arranged into a diamond shape to avoid the overlapping of the Raman spectra on the CCD camera. Similar for $R = 16$ pattern but the number of beam was restricted to 4 due to limited field-of-view (FOV) of the optical system. The pinhole size was ~92 μm on the DMD (608 × 684 pixels), which was approximately 1.5 units of the Airy diameter for the 60×/1.2 NA objective and L3 lens. The number of beams was fixed at 9, which was the optimal for the FOV of the current instrument. Figure 2d–g shows the original Raman CCD images of a uniform polystyrene slide measured using the four different multifoci laser patterns. Single-beam confocal Raman spectrum and CCD image are shown in Figure 2b,c, for reference. The intensity variation between the beams was different for different laser foci pattern. For line patterns (Figure 2d,e), the variation was around 5%. In the case of diamond-shaped pattern (Figure 2f,g), the intensity variation among the beams was more significant, with ~10% variation on the edge of FOV. The signal cross-talk among adjacent beams in the multifoci configuration is the main factor that decreases the depth discrimination because each laser foci have similar waists regardless of the pattern. Figure 2h shows a simple model for the overlapping volume of laser intensity where cross-talk could begin, starting at a critical depth in the sample, h_0, which is determined by the NA of objective and distance D between foci: $h_0 = D/2\tan\theta$. A lower value of h_0 would indicate a higher level of overlapping between adjacent laser foci.

To reveal the influence of confocal foci patterns on the depth discrimination in a systematic and quantitative manner, depth response curves of the foci patterns were obtained by measuring Raman spectra of a thick layer of oil on a quartz slide (Figure 3). Raman spectra were acquired at different focal planes by moving the sample in the axial direction (z-axis) in 10-μm steps. The depth response curves were then obtained by integrating the Raman bands corresponding to oil at 1,268 cm^{-1} (C=C symmetric rocking), 1,302 cm^{-1} (methylene twisting), 1,442 cm^{-1} (CH_2 scissoring), and 1,660 cm^{-1} (C=C stretching). The first derivatives of the response curves were fitted with a Gaussian function to calculate the full width at half maximum (FWHM). Figure 3b–d shows that, starting from the single laser beam configuration,

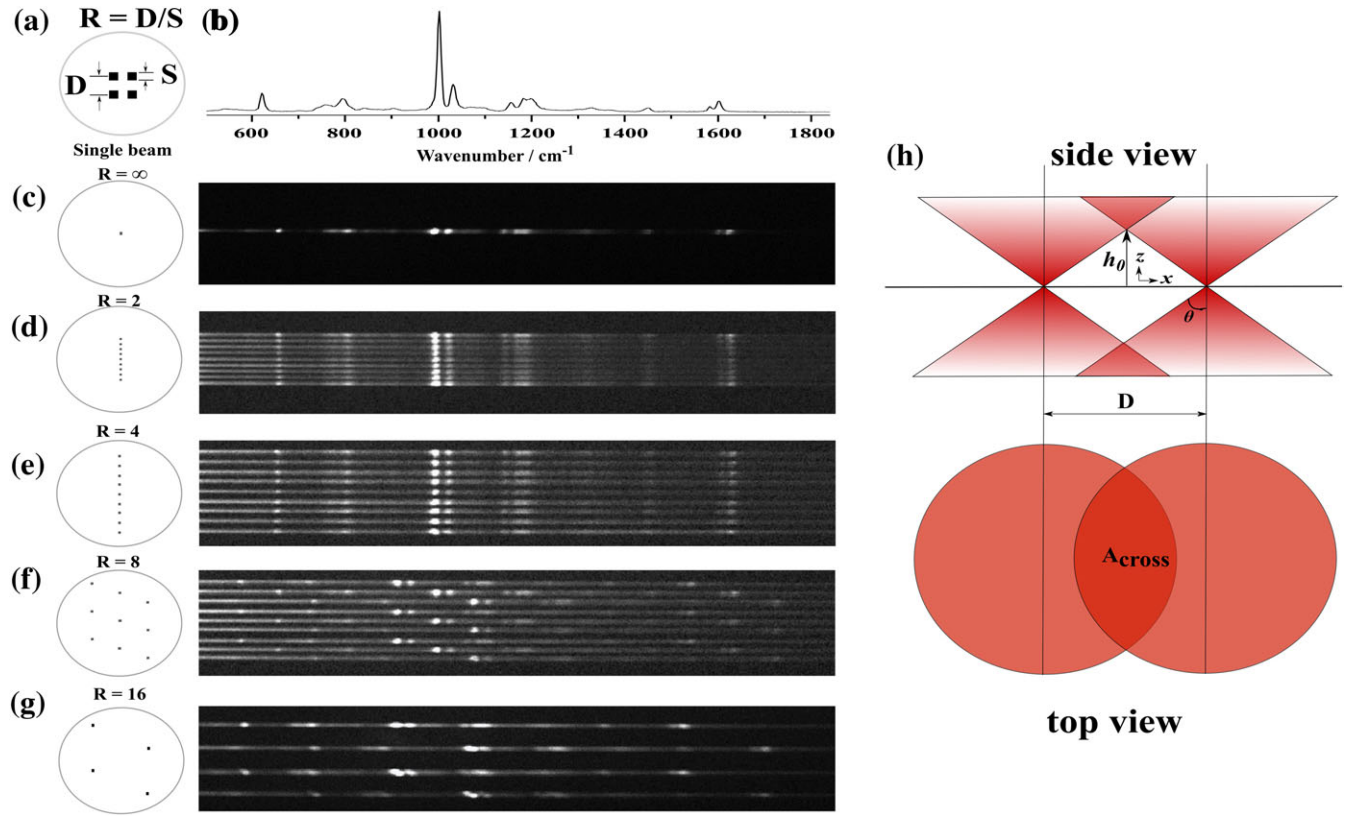

FIGURE 2 Spatial light modulator and digital micromirror device patterns used for multifocal Raman hyperspectral imaging. Corresponding Raman charge-coupled device images of uniform polystyrene slide acquired by using the patterns shown on the left. (a) Schematic of confocal pattern period, R refers to the distance-to-size ratio of adjacent pinholes. (b) Raman spectrum of polystyrene. (c) Single beam, $R = \infty$; (d) nine beams in a line, $R = 2$ confocal pattern period; (e) nine beams in a line, $R = 4$ confocal pattern period; (f) nine beams in an array, $R = 8$ confocal pattern period; (g) four beams in an array, $R = 16$ confocal pattern period; (h) Schematic of the signal cross-talk among beams in multifoci configuration. D denotes the distance between beams; h_0: critical height for cross-talk; A_{cross}: cross-talk area; θ: half-angular aperture [Colour figure can be viewed at wileyonlinelibrary.com]

the FWHM values increase gradually when the distance-to-size ratio decreases from $R = 16$ to $R = 2$. The degradation in depth discrimination is explained by the increase in cross-talk between adjacent beams, as indicated by the values of the critical value h_0, which decreases from $h_0 = 4.32$ μm for $R = 16$ to $h_0 = 0.54$ μm for R = 2.

While the results in Figure 3 indicate that the multifoci configuration of $R = 16$ provides better depth discrimination compared with the other patterns, the speed advantage of this configuration is reduced by the FOV of the objective, which limits the number of laser foci to 4. An $R = 16$ configuration with nine beams can also be achieved with the diamond-shaped pattern by reducing the pinhole size to half (~0.75 unit of the Airy disc). The calculated FWHM = 40 μm for the depth response curve (see Figure S2) shows that the depth discrimination decreases slightly compared with FWHM = 35 μm for the $R = 16$ with four beams. In addition, the speed advantage of this configuration is lost because of the need to reduce the size of the pinholes, which leads to a need to increase the integration time for each spectrum. Considering these arguments, we concluded that the optimal configuration for practical applications is the configuration $R = 8$ with nine beams, which provides an FWHM = 45 μm while opening the pinholes at 1.5 unit of the Airy discs. Furthermore, the critical depth value for this configuration is $h_0 = 2.16$ μm, which indicates that this configuration is well suited for our intended applications (i.e., hyperspectral imaging of nanomaterials and cells).

Next, we investigated the effect of the laser-foci pattern period on the depth discrimination of the depth-resolved Raman images. As a model sample, stacked FF microtubes were used. A group of images in Figure 4 shows that the depth discrimination varies as function of confocal pattern period. Details about how the Raman images were reconstructed are provided in the Supporting Information (see Figure S1. The area of the Raman band at 1,001 cm^{-1} assigned to phenyl symmetric ring breathing mode was used for the images. The Raman images are based on the data of 24 × 24 pixel images from each of the nine beams with step size of

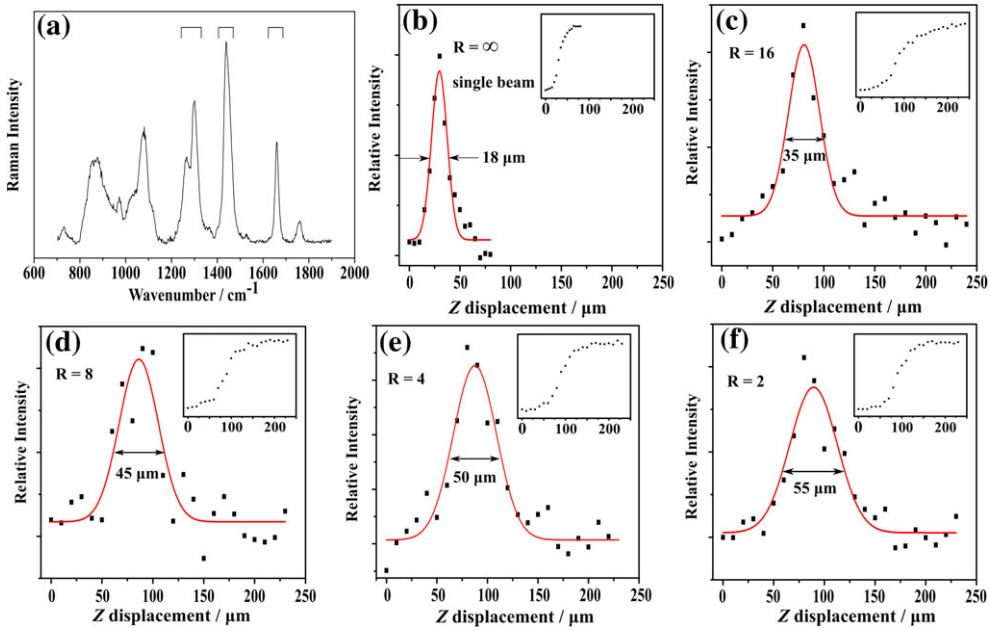

FIGURE 3 (a) Raman spectrum of oil after background subtraction. Bands used to obtain depth response curves for the Raman system are denoted with brackets. Calculated FWHM for the configuration of single beam with (b) $R = \infty$, (c) $R = 16$ with four beams, (d) $R = 8$, (e) $R = 4$, and (f) $R = 2$ with nine beams, respectively. Raw data of the response curves are shown in the insets. FWHM obtained from the first derivatives of the response curves and fitted with Gaussian function [Colour figure can be viewed at wileyonlinelibrary.com]

0.5 μm and cropped to 48 × 40 pixels to match the area from the single-beam Raman image; see Figure S1. The intensity variations among the nine beams were compensated in the process of reconstruction based on the Raman intensity CCD images shown in Figure 2. The exposure time was 0.2 s, and the total measurement time of each confocal plane was ~172 s for all three configurations. For comparison, the single-beam optical section in Figure 4b required a total measurement time of 1,036 s to map the same area. The multifoci measurement provided a speed up by a factor of 6. Figure 4a shows the bright-field image and a typical Raman spectrum of the FF microtubes. Figure 4b shows the single-beam confocal Raman images of the tubes at different focal planes. The data show that the Raman signal from the small FF tube decreased gradually as the focal plane moved from 0 to +2 μm, as shown in the cross-sectional traces, indicating that the thicker tube was above the thinner one. Figure 4c shows the Raman images of the FF tubes acquired with multifocal excitation using the $R = 2$ confocal pattern period arranged in a straight line. The Raman spectral images from different focal planes do not show clear depth features, as there is no significant change in the amplitude of the trace across the tube, indicating low depth discrimination for the $R = 2$ period. When the confocal pattern period was increased to $R = 4$, despite some residuals from the thin tube at depth of +2 μm, the depth features became clearer, as indicated by the changes in the amplitude of the trace across the FF tube (Figure 4d). With the $R = 8$ period diamond configuration, the depth-resolved images provided even better depth discrimination as the Raman photons of the thinner FF microtube can no longer be detected in the image corresponding to the +2 μm plane (Figure 4e). Although line multifoci configuration with $R = 8$ could provide similar depth discrimination as the diamond pattern, the latter has the advantage of allowing more laser spots to be fitted within the FOV. With this configuration, the advantages of confocal depth discrimination are made compatible with the increased throughput of multifocal sampling approaches, with additional flexibility afforded by the LC-SLM/DMD combination. The LC-SLM provided ~90% efficiency for light modulation (loss of laser power at the sample plane was mainly due to the requirement of overfilling the SLM active area and the back aperture of the objective), enabling us take full advantage of the high power output from the Ti:Sapphire laser.

Figure 5a shows a stack of images of the volume structure of the FF microtubes obtained using the $R = 8$ confocal pattern period. Images were acquired at seven different confocal planes with a depth step size of 1 μm. Raman photons from the thinner FF tube were detected only in the first few measurement slices. When the depth increased to over 4 μm, Raman photons from the thin FF tube were no longer detected, demonstrating the capability of multifocal Raman imaging for optical

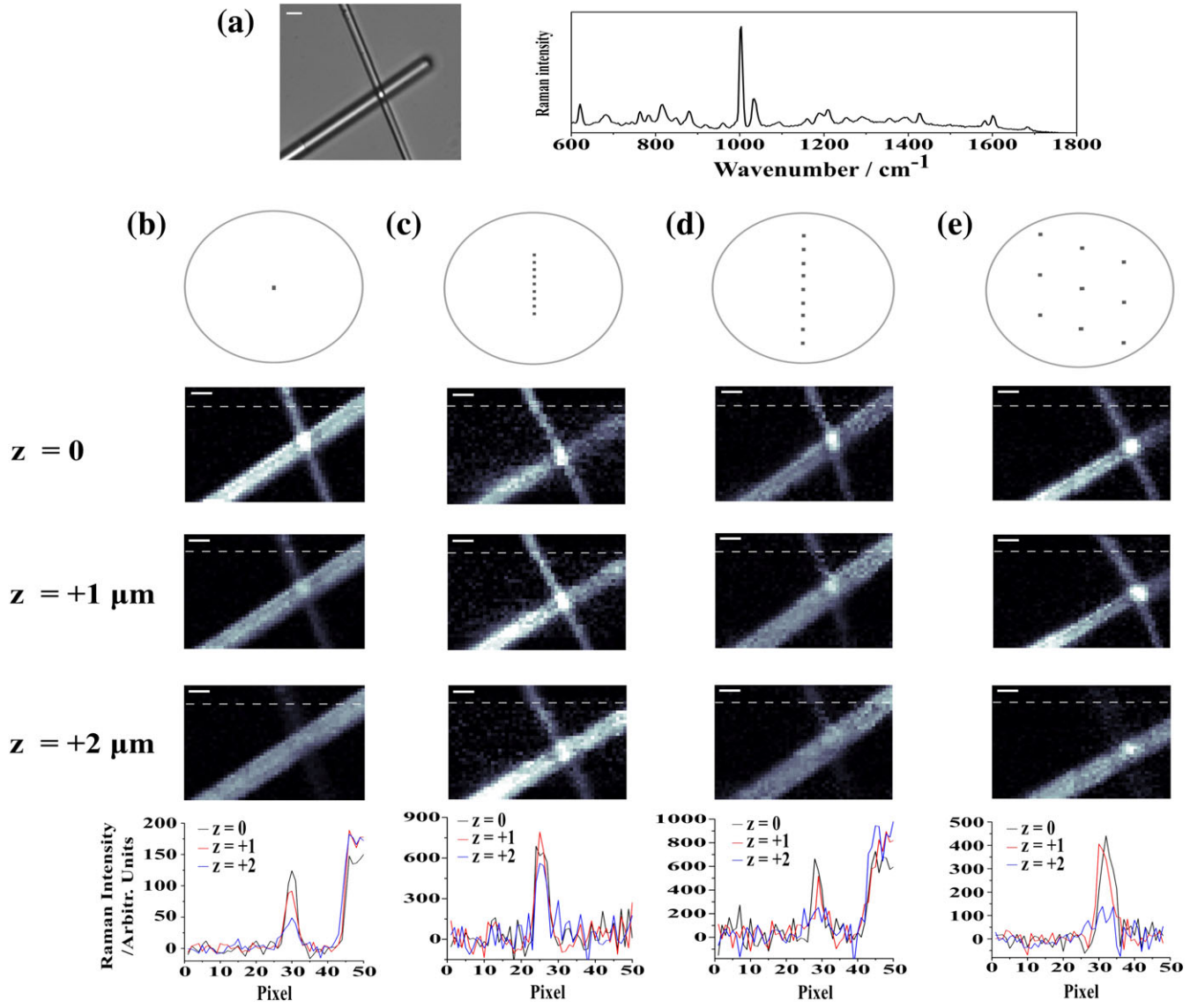

FIGURE 4 Raman imaging of diphenylalanine microtubes at different focal planes (z = 0, 1, 2 μm) using different configurations. The images were obtained using the intensity of the phenyl ring breathing mode Raman band at 1,001 cm^{-1}. (a) Wide-field image and Raman spectrum of the diphenylalanine microtube; (b) single-beam confocal Raman mapping; (c), (d), and (e) multifoci Raman images obtained using the confocal pattern shown on the top; dashed lines mark the cross sections shown in the plots on the bottom. Scale bars, 3 μm [Colour figure can be viewed at wileyonlinelibrary.com]

sectioning. Figure 5b displays a projection of the 3D volumetric structure (reconstructed using ImageJ 3D Viewer). Another example of multifoci Raman imaging for optical sectioning is shown in Figure S3, in which a cotton fiber immersed in water was imaged with R = 8 confocal pattern period. The irregular surface of the fiber was revealed by the Raman images at different confocal planes.

In order to demonstrate the capability of multifoci Raman imaging for optical sectioning of biological materials, *A. castellanii* trophozites cultured on a quartz slide were scanned with the multifoci Raman microspectrometer using nine beams diamond-shaped pattern with R = 8 confocal period. This configuration is well suited for depth-resolved imaging of the cells as the thickness of the cells is similar to the critical depth value h_0 = 2.16 μm. Figure 6a shows the bright-field image of two cells. Singular value decomposition was used to reduce noise in the raw spectra, using the first latent values for spectral reconstruction.[21] Spectra acquired from each of the nine beams were processed separately to avoid artifacts caused by errors in the spectral calibration. Figure 6b displays the Raman spectral images generated using the integrated intensity of CH_2 deformation band at 1,450 cm^{-2} after background subtraction. The Raman images from different focal positions reveal the subcellular structure within the trophozites. As the depth increased from z = 0 to

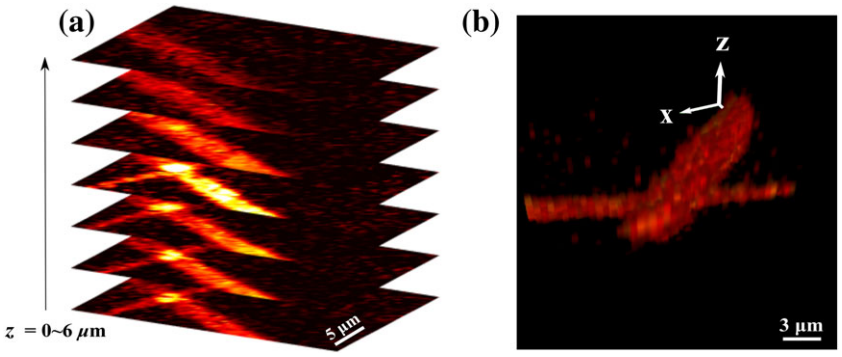

FIGURE 5 Optical sectioning by multifoci Raman imaging of diphenylalanine microtubes. (a) A stack of images acquired at different z-planes. (b) Three-dimensional image of the volume structure

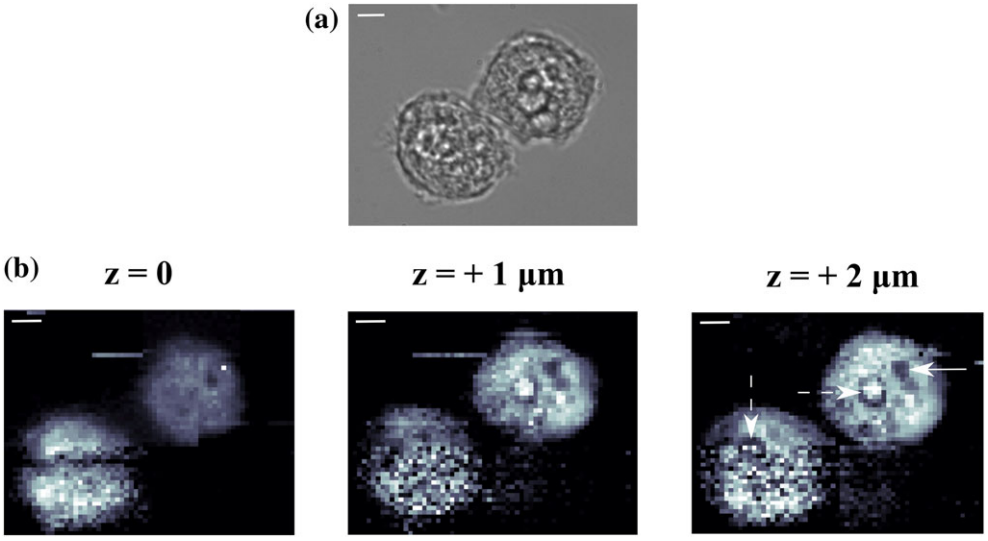

FIGURE 6 Raman imaging of *Acanthamoeba castellanii* trophozites using the 8 × 8 period confocal pattern. (a) Bright-field image of trophozites fixed on quartz slide. (b) Raman spectral images of the trophozites obtained at three different confocal planes using the 8 × 8 period confocal pattern. Three principal components were used for the reconstruction of spectra. Raman images were obtained by integrating the intensity under the CH_2 deformation band at 1,450 cm^{-2} after background subtraction. The nucleus and the contractile vacuole are indicated by dashed and solid arrows, respectively. Scale bars, 3 μm [Colour figure can be viewed at wileyonlinelibrary.com]

z = +2 μm, the Raman intensity from the top-right trophozoite also increased gradually, and the structure of the nucleus and the vacuole become more distinguishable (Figure 6b).

The images were obtained by collecting Raman spectra with nine beams simultaneously at an interval of 0.5 μm and 24 × 24 points for each beam. An area of ~36 × 36 μm^2 was covered by a single scan. A total laser power of ~300 mW at the sample plane was shared by the nine beams, resulting in roughly 30 mW per beam for Raman excitation (some power remained in the 0th order spot, which was not used for imaging). The integration time for the Raman spectra was 2 s, leading to a total measurement time of ~1 hr to complete. Although 3D Raman spectral imaging based on single-point laser excitation was reported previously,[22] the multifoci excitation approach provides a clear speed advantage while maintaining a high depth discrimination.

4 | CONCLUSION

We have employed a multifoci Raman microscope based on a LC-SLM for laser excitation and a DMD for confocal Raman detection to investigate the effect of the confocal period (ratio between pinhole spacing and pinhole diameter) on depth discrimination. The multifoci laser patterns included 1D (line) and 2D (diamond shape) patterns. The software controlling the LC-SLM and DMD of the instrument allowed the rapid and flexible changes to the patterns and confocal period. Four multifoci confocal patterns with different periods, from R = 2 line, R = 4 line, R = 8 diamond, and R = 16 diamond shape, have been employed for Raman imaging. Experiments on thick transparent sample enabled a better understanding of the effects of laser foci overlap and Raman signal cross-talk on the spectral depth discrimination. For samples with thicknesses similar to the critical depth h_0 (1–3 μm), results from optical sectioning of FF microtubes

suggested that an $R = 8$ period was optimal for maintaining depth discrimination while maximizing imaging speed. For applications where smaller confocal period could be used, more beams in the FOV of the current system can be easily achieved, as the SLM/DMD provides great flexibility that allows the choices of throughput versus depth discrimination.

ACKNOWLEDGMENT

This work was supported by the Engineering and Physical Sciences Research Council [grant number EP/L025620/1, EP/M506588/1], the first grant through the Established Career Fellowship and the second grant through the Doctoral Prize.

ORCID

Zhiyu Liao http://orcid.org/0000-0002-6447-5510
Faris Sinjab http://orcid.org/0000-0001-9932-9786
Hany M. Elsheikha http://orcid.org/0000-0003-3303-930X
Ioan Notingher http://orcid.org/0000-0002-5360-230X

REFERENCES

[1] D. W. Shipp, F. Sinjab, I. Notingher, *Adv. Opt. Photon.* **2017**, *9*, 315.

[2] J. Qi, W.-C. Shih, *Appl. Opt.* **2014**, *53*, 2881.

[3] K. Watanabe, A. F. Palonpon, N. I. Smith, L. D. Chiu, A. Kasai, H. Hashimoto, S. Kawata, K. Fujita, *Nat. Commun.* **2015**, *6*, 10095.

[4] D. Wei, S. Chen, Y. H. Ong, C. Perlaki, Q. Liu, *Opt. Lett.* **2016**, *41*, 2783.

[5] L. V. Doronina-Amitonova, I. V. Fedotov, A. B. Fedotov, A. M. Zheltikov, *Appl. Phys. Lett.* **2013**, *102*, 161113.

[6] M. Okuno, H.-o. Hamaguchi, *Opt. Lett.* **2010**, *35*, 4096.

[7] L. Kong, P. Zhang, J. Yu, P. Setlow, Y.-q. Li, *Appl. Phys. Lett.* **2011**, *98*, 213703.

[8] J. Qi, W.-C. Shih, *Opt. Lett.* **2012**, *37*, 1289.

[9] A. Z. Samuel, S. Yabumoto, K. Kawamura, K. Iwata, *Analyst* **2015**, *140*, 1847.

[10] M. Navas-Moreno, J. W. Chan, *Opt. Lett.* **2017**, *42*, 37.

[11] Y. Kumamoto, Y. Harada, H. Tanaka, T. Takamatsu, *Sci. Rep.* **2017**, *7*, 845.

[12] S. Yabumoto, H.-o. Hamaguchi, *Anal. Chem.* **2017**, *89*, 7291.

[13] L. Kong, M. Navas-Moreno, J. W. Chan, *Anal. Chem.* **2016**, *88*, 1281.

[14] L. Kong, J. Chan, *Anal. Chem.* **2014**, *86*, 6604.

[15] F. Sinjab, K. Kong, G. Gibson, S. Varma, H. Williams, M. Padgett, I. Notingher, *Biomed. Opt. Express* **2016**, *7*, 2993.

[16] Z. Liao, F. Sinjab, G. Gibson, M. Padgett, I. Notingher, *Opt. Express* **2016**, *24*, 12701.

[17] Z. Liao, F. Sinjab, A. Nommeots-Nomm, J. Jones, L. Ruiz-Cantu, J. Yang, F. Rose, I. Notingher, *Anal. Chem.* **2017**, *89*, 847.

[18] F. Sinjab, G. Bondakov, I. Notingher, *Appl. Phys. Lett.* **2014**, *104*, 251905.

[19] A. Naemat, F. Sinjab, A. McDonald, A. Downes, A. Elfick, H. M. Elsheikha, I. Notingher, *J. Raman Spectrosc.* **2018**, *49*, 412.

[20] R. W. Bowman, G. M. Gibson, A. Linnenberger, D. B. Phillips, J. A. Grieve, D. M. Carberry, S. Serati, M. J. Miles, M. J. Padgett, *Comput. Phys. Commun.* **2014**, *185*, 268.

[21] A. Ghita, F. C. Pascut, M. Mather, V. Sottile, I. Notingher, *Anal. Chem.* **2012**, *84*, 3155.

[22] K. Majzner, A. Kaczor, N. Kachamakova-Trojanowska, A. Fedorowicz, S. Chlopicki, M. Baranska, *Analyst* **2013**, *138*, 603.

SUPPORTING INFORMATION

Additional supporting information may be found online in the Supporting Information section at the end of the article.

How to cite this article: Liao Z, Sinjab F, Elsheikha HM, Notingher I. Optical sectioning in multifoci Raman hyperspectral imaging. *J Raman Spectrosc*. 2018;1–8. https://doi.org/10.1002/jrs.5450